remote sensing

MDPI

Technical Note

Simulation and Assessment of Daily Evapotranspiration in the Heihe River Basin over a Long Time Series Based on TSEB-SM

Sinuo Tao [1], Lisheng Song [2,*], Gengle Zhao [1] and Long Zhao [1]

[1] School of Geographical Sciences, Southwest University, Chongqing 400715, China; tsn876@email.swu.edu.cn (S.T.); lele1120@email.swu.edu.cn (G.Z.); zhaol04@swu.edu.cn (L.Z.)
[2] School of Geography and Tourism, Anhui Normal University, Wuhu 241002, China
* Correspondence: songls@ahnu.edu.cn

Abstract: The high spatial and temporal resolution of recently developed evapotranspiration (ET) products facilitates agricultural water-savings in irrigated areas as well as improved estimates of crop yield, especially in arid and semi-arid regions. However, cloud cover interferes with ET estimates, in particular when using thermal-infrared-based models in temperate and tropical regions. Previous studies have shown that the two-source energy balance (TSEB) model coupled with soil moisture (TSEB-SM) has great potential for estimating surface ET by overcoming this issue. In this study, the TSEB-SM model was first used to generate a spatiotemporally continuous 1 km daily ET dataset across the Heihe River Basin in China from 2000 to 2020, which was then evaluated against four spatially distributed sites (Arou, Huazhaizi, Daman, and Sidaoqiao) and further compared with the two most widely used daily ET datasets (PML-V2 (Penman–Monteith–Leuning) and SEBAL (surface energy balance algorithm for land)). The results showed that the newly developed ET dataset agrees well with ground-based observations and outperforms the PML-V2 and SEBAL products in precisely characterizing the seasonal fluctuations and spatial distribution as well as the spatiotemporal trends of ET. In particular, ET in the Heihe River Basin exhibits clear regional differences. The upstream and midstream grassland and irrigated oasis areas provide much higher annual ET than the downstream desert areas, with a difference of up to 600 mm/year. A three-cornered hat (TCH)-based pixel-by-pixel analysis further demonstrated that the TSEB-SM and PML-V2 products have substantially smaller relative uncertainties as compared to SEBAL ET. In general, the proposed ET datasets are expected to be more beneficial for irrigation scheduling and to provide more efficient water management across the Heihe River Basin.

Keywords: ET; TSEB-SM; TCH; model; Heihe River Basin

Citation: Tao, S.; Song, L.; Zhao, G.; Zhao, L. Simulation and Assessment of Daily Evapotranspiration in the Heihe River Basin over a Long Time Series Based on TSEB-SM. *Remote Sens.* **2024**, *16*, 462. https://doi.org/10.3390/rs16030462

Academic Editors: Dongryeol Ryu, Hao Sun and Liangliang Tao

Received: 15 December 2023
Revised: 18 January 2024
Accepted: 23 January 2024
Published: 25 January 2024

1. Introduction

Land surface evapotranspiration (ET) consists mainly of evaporation (E) from soil and vegetation surfaces and transpiration (T) from plant canopies; these are all linked to the water, energy, and carbon cycles [1]. Studies have shown that around 58–65% of precipitation returns to the atmosphere through terrestrial ET, and that transpiration of vegetation accounts for more than 65% of terrestrial ET [2]. When converted to energy, this ET is equivalent to 51–58% of the incident energy due to ambient net radiation [3]. As a result, ET plays an important role in determining regional and global water balances and strongly influences the development of complex regionally coupled hydrology, ecology, and atmospheric systems [1]. The accurate estimation of ET is crucial not only for the study of the global and regional effects of climate change [4,5], but also for studying resource utilization, crop yield prediction, drought monitoring, and weather forecasting [6].

Generally, ET is measured on the ground using field lysimeters, eddy covariance systems and large-aperture scintillometers, providing spatial representatives from hundreds of meters to several kilometers. The instrumental techniques mentioned above may only be used at the appropriate spatial scales, which are generally small [7]; many are campaign mode, and the observations are hard to extend to larger regions, such as watersheds, due to the typically strong spatial heterogeneity in vegetation transpiration and soil evaporation. Therefore, ground-based observations are insufficient to fulfill the needs of estimating regional- and global-scale ET. With the development of remote sensing technology, surface model simulations based on remote sensing data have proven to be an excellent method for estimating ET at regional to global scales [8–10].

A large number of remote-sensing-modeled ET datasets have been released, over a wide range of spatial and temporal scales. For instance, some of the available global-scale data, with a temporal resolution of 8 days and spatial resolution from 500 to 1000 m, include MOD16 (the Moderate-Resolution Imaging Spectroradiometer, spanning 2000–present), an important terrestrial ET product based on a modified Penman–Monteith approach. The effect of soil moisture in MOD16 is indirectly expressed through relative humidity (RH), vapor pressure deficit (VPD), and leaf area index (LAI), resulting in uncertainty in regional ET estimation. PML-V2 (Penman–Monteith–Leuning) (spanning 2000–2020) couples transpiration of vegetation with GPP (gross primary productivity) according to the stomatal conductance theory, and the parameters in PML-V2 are rate-determined from observations at 95 eddy-related flux stations around the globe and extended by vegetation type. In this way, the PML-V2 model was able to efficiently estimate the effect of increasing atmospheric CO_2 concentration on ET [11]. The GLASS (Global Land Surface Satellite) ET dataset was produced by merging five process-based ET algorithms, adopting the concept of algorithmic aggregation with high accuracy [12]. Although the above datasets can meet the spatial precision needs of ET analysis at the watershed scale, the 8-day temporal scale is too coarse to make timely, informed irrigation management decisions for agriculture. Despite the availability of ET products with high temporal resolution—such as the daily ET product GLEAM (Global Land Evaporation Amsterdam Model), for instance, which calculates potential evaporation by the Priestley–Taylor formula based on observations of surface net radiation and near-surface air temperature—these cannot be used for field-scale ET analysis, because the spatial resolution is too coarse at $0.25^\circ \times 0.25^\circ$. Concurrent high-spatial- and –temporal-resolution ET products need to properly depict spatial and temporal ET variation in catchments, and the minimum requirement for this is daily ET datasets with 1 km spatial resolution, as these are then conducive to field-scale water management.

The Heihe River Basin is a pivotal water resource in China for maintaining the existence and socioeconomic development of the so called "oasis" in the Hexi Corridor, an area that has a dry climate, scarce precipitation, and depleted groundwater [13,14]. The major demands on water in the Heihe River Basin are due to plant transpiration and soil evaporation. In recent years, poorly regulated irrigation has led to serious deterioration of the water resources in the Heihe River Basin [14]. Concomitant with this has been a marked reduction in the available water supply for agriculture due to drought. Hence, there is a pressing need for daily ET products at the field and watershed scales to help local governments to develop reasonable irrigation and water conservation measures. A number of simulation experiments on ET have been carried out in the Heihe River Basin. Yang et al. [15] conducted field observations of ET from grasslands in the upstream of the Heihe River, and they evaluated the FAO–Penman–Monteith (FAO-PM), Priestley–Taylor (PT), and Hargreaves–Samani (HS) models based on their observations, noting that the PT model yielded the highest accuracy in estimating daily ET. Song et al. [16] evaluated the adaptability of Penman–Monteith (PM), ASCE–Penman–Monteith (ASCE-PM), and Priestley–Taylor (PT) models for grassland in the upstream of the Heihe River by using observations, and the results showed that the PM model was the most effective for estimating ET in grassland. Due to the higher surface heterogeneity and the climatic conditions in the Heihe River Basin, this model is more demanding. TSEB (two-source energy balance) is a more physical-based model using satellite-based thermal infrared (TIR) to obtain surface ET data, while the TSEB-SM (two-source energy balance–soil moisture) model is an enhanced version of TSEB that incorporates a surface soil water stress index into its coupled evaporation and transpiration algorithm. Specifically, the TSEB-SM model initially computes the surface soil water stress index to capture both soil dryness and plant transpiration. Subsequently, this index is considered alongside other factors, such as surface temperature and vegetation type, to more accurately estimate the soil evaporation and plant transpiration rates. The TSEB-SM model can effectively handle study areas across a wide range of soil moisture conditions, from fully saturated to extremely arid soils, thereby providing improved accuracy in estimating both soil evaporation and plant transpiration.

The aims of this study were to (1) simulate the daily surface ET in the Heihe River Basin from 2000 to 2020 based on the TSEB-SM model, (2) evaluate the accuracy of the simulation results directly with ground-based observations and indirectly with the TCH (three-cornered hat) method in combination with daily PML-V2 ET and SEBAL (Surface Energy Balance Algorithm for Land) ET data, and (3) characterize the spatial and temporal patterns of surface ET in the Heihe River Basin from 2000 to 2020.

2. Study Area and Data

2.1. Study Area

The Heihe River Basin is the second-largest inland basin in the region of Northwest China (97.12°E–102.08°E, 37.73°N–42.74°N), with hot summers and cold winters. As is characteristic of arid and semi-arid environments, the region has little and irregularly distributed precipitation, primarily in the summer. Due to human interference and the local drought-prone climate, the ecological balance is delicate. The vast regional coverage, differing climate, and terraced terrain, extending from the upstream to the downstream, combine to create the rich and varied natural landscape of the Heihe River Basin. The upstream is dominated by alpine meadows, the midstream is primarily made up of artificial oases and irrigated areas, and the downstream is mostly covered by the Gobi Desert, except for a small stretch of riparian forests along the Heihe River. The Heihe River Basin is heavily dependent on water resources because of predominantly irrigated agriculture, and as cities and industries expand, so does the demand for water resources. The development of the Heihe River is time-honored, and human activities have significantly affected its ecological environment. The abovementioned characteristics make the Heihe River Basin an ideal region for conducting integrated watershed studies. The land cover and the locations of the flux towers selected for the evaluation are shown in Figure 1.

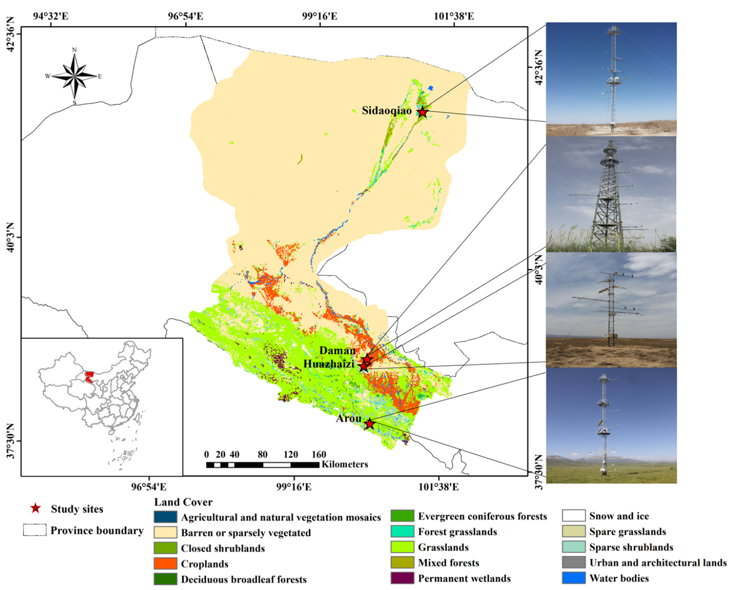

Figure 1. Location of the Heihe River Basin and four EC flux towers at Arou, Huazhaizi, Daman, and Sidaoqiao. The background shows the land cover of the Heihe River Basin and its surrounding areas.

2.2. Model Input Data

The TSEB-SM model can be driven by land surface temperature (LST), leaf area index (LAI), soil moisture (SM), land cover, and meteorological forcing data.

One of the most important model factors is LST, which will be divided into two categories here: soil temperature and vegetation. The model's simulation performance is greatly impacted by the precision of LST. However, cloud and fog contamination cause the satellite's thermal infrared (TIR) LST product to be discontinuous. Zhang et al. [17] introduced a practical reanalysis data and thermal infrared remote sensing data merging (RTM) method for generating all-weather LST data at 1 km spatial resolution by merging reanalysis data and TIR LST output. The above LST data at 1 km spatial resolution across the Heihe River Basin were downloaded from the Central Tibetan Plateau Data Center (https://www.tpdc.ac.cn/en/, accessed on 18 January 2022).

Another important parameter is LAI, which is mainly used to separate the surface fluxes and LST between the soil and canopy. The daily LAI maps over the Heihe River Basin were derived from the 8-day global 500 m GLASS LAI product from 2000 to 2020 [18]. The Heihe River Basin crosses a wide region and often includes three MODIS remote sensing images, namely, h25v04, h25v05, and h26v05. After stitching these three images and clipping them according to the scope of the study area, the treated LAI was then resampled and temporally interpolated to ensure consistency with other data in terms of spatial and temporal resolution.

In order to identify different vegetation types to assign height empirically, the Terra and Aqua combined Moderate-Resolution Imaging Spectroradiometer (MODIS) Land Cover Climate Modeling Grid (CMG) (MCD12C1) Version 6 data product at $0.05^{\circ} \times 0.05^{\circ}$ spatial resolution was used. Based on the nearest-neighbor resampling method, we downscaled it to 1 km spatial resolution.

The meteorological data input to the model, including air temperature, relative humidity, atmospheric pressure, shortwave radiation, and wind speed, were simulated by the weather research and forecasting (WRF) model [19]. The WRF model makes up for the deficiency of general circulation models (GCMs) at the watershed scale, especially the coarse spatial resolution. Verified by the hourly ground-based observations, the 5 km hourly WRF meteorological forcing data show a great agreement with them. These datasets were downloaded from the Central Tibetan Plateau Data Center (https://www.tpdc.ac.cn/en/, accessed on 25 December 2021).

2.3. Observation Data

Ground-based observations were downloaded from the Central Tibetan Plateau Data Center (https://www.tpdc.ac.cn/en/, accessed on 27 January 2022) and originated from the Integrated Observation Network for Surface Processes in the Heihe River Basin. The comprehensive observation network of surface processes in the Heihe River Basin utilizes a variety of advanced observation equipment, including automatic weather stations, moisture monitors, and eddy covariance systems, and combines the monitoring means of many disciplines, such as meteorology, hydrology, ecology, and geography, so as to achieve all-round observation of surface processes in the basin. The observations include meteorological parameters such as temperature, humidity, wind speed, and precipitation, along with remotely sensed parameters such as vegetation index and surface temperature. The observation network covers the whole basin of the Heihe River, and in this study, the Arou site located in the upstream alpine meadows (100.46°E, 38.05°N), the Daman site in the middle reaches of the irrigation area (100.37°E, 38.86°N), the Huazhaizi desert site (100.32°E, 38.77°N), and the Sidaoqiao site (101.14°E, 42.00°N) located in the downstream riparian forest were selected. The observations of the meteorological stations included air temperature, air humidity, barometric pressure, soil moisture, and other parameters. The three soil heat flux panels were mounted two meters due south of the meteorological tower to observe the soil heat fluxes. The sensible and latent heat fluxes were observed by the eddy covariance systems, with a sampling frequency of 10 Hz. Typically, eddy covariance systems underestimate sensible and latent heat fluxes due to site characteristics [20], which may partially affect the research findings. As such, the energy balance closure had values ranging from 0.80 to 1.05, which were forced using the Bowen ratio approach.

2.4. Remote Sensing Data

To further evaluate the ET accuracy of the TSEB-SM simulations, the daily ET datasets were selected for indirect cross-validation against the TSEB-SM ET data, that is, the PML-V2 ET data and the SEBAL ET data.

The PML_V2 [11] ET dataset has a spatial and temporal resolution of 0.05° and daily, respectively. It comprises vegetation transpiration (Ec), soil evaporation (Es), vaporization of intercepted rainfall (Ei), and evaporation from water and snow (ET_water). In order to improve the simulation accuracy, vegetation transpiration and GPP were coupled based on the Penman–Monteith–Leuning (PML) model and stomatal conductivity theory. This balances GPP and Ec, improving the effect of increasing atmospheric CO_2 concentration on carbon and water processes. The observations of 95 eddy covariance flux sites worldwide were used to derive the PML_V2 parameter, which was then extended to the entire planet based on vegetation types. The final step was to obtain the datasets for terrestrial ET and total primary productivity by using the meteorological drivers of GLDAS 2.1 and MODIS reflectance (albedo), emissivity (emissivity), leaf area index (LAI), and continuous dynamic vegetation type (MODIS MCD12Q2.006 IGBP) as inputs to PML V2. The PML-V2 data were downloaded from the Central Tibetan Plateau Data Center (https://www.tpdc.ac.cn/en/, accessed on 17 July 2022). The SEBAL ET dataset (2001–2018) is based on the Surface Energy Balance Algorithm for Land, with a spatial and temporal resolution of 1 km × 1 km and daily, respectively. SEBAL is an advanced algorithm utilized to estimate the land surface ET [21]. This algorithm is grounded in the principle of energy balance, where the incoming energy (comprising solar and atmospheric radiation) to the Earth's surface must be balanced by the sum of sensible heat flux (heat transferred to the air), latent heat flux (evaporation of water), and ground heat flux (heat transferred into the soil). The SEBAL model calculates the instantaneous λET of the satellite transit time as a residual based on the surface energy balance equation. The daily surface ET is then obtained by an upscaling algorithm. The SEBAL ET data for this study used MCD43 surface albedo, MOD11 surface temperature, MOD13 NDVI, and meteorological data (air temperature) from the Global Modeling and Assimilation Office (GMAO) as input data.

3. Methods

3.1. TSEB-SM

The TSEB model, first proposed by Norman et al. [22], is a widely used approach to simulate surface flux with various land cover types [23–25]. It is based on the energy balance principle, which can be described as follows:

$$\boldsymbol{R_n \approx H + LE + G} \tag{1}$$

$$\boldsymbol{R_{n,s} \approx H_S + LE_S + G} \tag{2}$$

$$\boldsymbol{R_{n,c} \approx H_C + LE_C} \tag{3}$$

where R_n is the net radiation (i.e., incoming radiation minus outgoing radiation), H is the sensible heat flux, LE is the latent heat flux, and G is the soil heat flux. The subscripts C and S refer to the canopy and soil, respectively. Due to some additional flux that we always neglect, such as heat advection, the symbol "≈" is used here.

The critical process in the TSEB model is partitioning surface radiometric temperature (namely, T_{rad}) into soil and canopy temperature, which can be achieved by Equation (4):

$$\boldsymbol{T_{rad}^4(\theta) = f_C(\theta)T_C^4 + [1 - f_C(\theta)]T_S^4} \tag{4}$$

where θ is the view angle, $f_c(\theta)$ is the vegetation fractional cover at the viewing angle, T_c is the canopy surface temperature, and T_s is the soil surface temperature.

After that, sensible heat flux of the canopy and soil can be obtained using Equations (5) and (6), respectively:

$$H_C = \rho_{air} C_P \frac{T_S - T_{AC}}{R_X} \tag{5}$$

$$H_s = \rho_{air} C_P \frac{T_S - T_{AC}}{R_X} \tag{6}$$

where ρ_{air} is the density of the air (kg m^{-3}), C_P is the heat capacity of the air, T_{AC} is the air temperature in the canopy, R_X is the boundary layer resistance of the canopy, and R_S is the resistance of the boundary directly above the soil surface to heat flow.

Combining the Priestley–Taylor formula with the linearization approximation to the resistance approach, which is described in detail by Norman et al. [22], T_c was estimated using the following equations:

$$T_{ci} = T_a + \frac{R_{n,c} R_{ah}}{\rho C_P}\left(1 - \alpha_{PT} f_g \frac{g_{stress}}{g_a} \frac{\Delta}{\Delta + \gamma}\right) \tag{7}$$

$$T_s = T_a + \frac{(R_{n,s} - G_0)(R_{ah} + R_s)}{\rho C_P}\left(1 - \alpha_s f_s \frac{\Delta}{\Delta + \gamma}\right) \tag{8}$$

where T_{ci} is the initial vegetation temperature, T_a is the air temperature, $R_{n,c}$ is the soil net radiation, $R_{a,h}$ is the aerodynamic resistance of turbulent heat transfer between the reference height and measured height of the vegetation, α_{PT} is the Priestley–Taylor coefficient for vegetation (initially set to 1.26 [26], but when the soil moisture reaches saturation it will close to 2), f_g is the fraction of green vegetation, Δ is the slope of the saturation vapor pressure–temperature curve, γ is the psychrometric constant, f_s is the soil water stress factor to express the influence of water stress on soil evaporation, and g_{stress}/g_a is the plant transpiration factor [27].

The soil surface evaporation varies with soil moisture content; a soil water stress factor ($f_{s\text{-}song}$) was introduced to the TSEB model under a wet soil surface (an irrigated area in the growing season) by Song et al. [28], while an analogical factor ($f_{s\text{-}merlin}$) under dry conditions was also introduced by Merlin et al. [29] through the soil texture information. But both of the above factors have limitations in some way; the factor $f_{s\text{-}song}$ may lead to an underestimation of soil surface temperature, since it cannot restrict the process of water loss from the soil surface adequately when the soil surface moisture is near the field's capacity. To fill this gap, a new stress expression f_s was added, which covers the full range of soil water content. This compensates for the limitations of $f_{s-merlin}$ and f_{s-song}.

$$f_{s-song} = \frac{2}{1 + (\frac{\theta}{\theta_0})^{-2}} \tag{9}$$

$$f_{s-merlin} = \frac{1}{2} - \frac{1}{2} cos(\frac{\theta}{\theta_{max}}) \tag{10}$$

$$f_s = \sqrt{f_{s-song} f_{s-merlin}} \tag{11}$$

where θ is the water content in the soil layer, θ_0 *is* the soil moisture at wilting, and θ_{max} is the saturating soil moisture.

The canopy net radiation and soil net radiation can be calculated via Equations (12) and (13), respectively:

$$R_{n,c} = \left(1 - \tau_{longwave}\right)\left(L_{\downarrow} + \varepsilon_s T_s^4 - 2\varepsilon_c T_c^4\right) + (1 - \tau_{solar})(1 - \alpha_c) S_{\downarrow} \tag{12}$$

$$R_{n,s} = \tau_{longwave} L_{\downarrow} + \left(1 - \tau_{longwave}\right)\varepsilon_c T_c^4 - \varepsilon_s T_s^4 + \tau_{solar}(1 - \alpha_s) S_{\downarrow} \tag{13}$$

where τ is the radiation transmission rate, ε is the radiation emissivity, α is the albedo, the subscript *longwave* represents solar longwave radiation, *solar* represents solar shortwave radiation, $L_{\downarrow}$ is downward longwave radiation, and $S_{\downarrow}$ is downward shortwave radiation.

After that, based on the energy balance model, the latent heat flux of the soil and canopy can be calculated. The more details of TSEB-SM model is in Supplementary Materials.

3.2. Bowen Ratio Method

The turbulent pulsation values of the latent and sensible heat fluxes of the subsurface may be directly monitored and estimated to produce the ET of the subsurface based on the eddy covariance approach. However, there are still a lot of technical issues with the eddy covariance approach that need to be fixed, which cause inaccuracies in the observed turbulent fluxes. Eddy covariance is challenging to detect, especially at night when turbulence is weak, and the turbulence intensity directly influences energy closure, which can result in the phenomenon of energy non-closure (i.e., the sum of the sensible and latent heat fluxes is lower than the difference between the net radiation and soil heat fluxes), which understates ET. The Bowen ratio, i.e., the ratio of sensible to latent heat fluxes, was first proposed by Bowen [30] and is denoted by the following formula:

$$\boldsymbol{\beta = \frac{H}{LE}} \quad (14)$$

Using the Bowen ratio approach and the energy balance equation, assuming that the observed values of net radiation and soil heat flux are accurate but that the measured values of H and LE are both lower than the actual values, the LE can be retrieved.

$$\boldsymbol{LE = \frac{Rn - G}{1 + \beta}} \quad (15)$$

The EC observations at four ground sites (Arou, Daman, Huazhaizi, and Sidaoqiao) from 2014 to 2020 were revised through the Bowen ratio method and then were upscaled to daily ET to examine the accuracy of the model.

3.3. Three-Cornered Hat (TCH) Method

The TCH method was first proposed by Premoli and Tavella and Tavella and Premoli [31,32]. It is used for estimating the relative uncertainty of multiple time-series measurements, particularly when a true reference standard is not available. In this study, all 3 ET products had the same spatial resolution of 1 km × 1 km, and the TCH method was applied pixel by pixel in the Heihe River Basin to obtain the relative uncertainties.

Firstly, every ET sequence was split into two terms:

$$\boldsymbol{X_i = X_{true} + \varepsilon_i, i = 1, 2, \ldots, N} \quad (16)$$

where X_{true} represents the true value of ET, ε_i is the error of the ith ET time series, and N is the number of ET data.

Secondly, an arbitrary sequence was selected as a reference sequence, and the relative uncertainty was estimated by difference.

$$\boldsymbol{Y_{i,N} = X_i - X_N, i = 1, 2, \ldots, N - 1} \quad (17)$$

where Y is the M × (N − 1) dimensional matrix and M is the number of time-series phases. The selection of the reference field does not affect the relative uncertainty, so PML-V2 ET was chosen as the reference field in this paper. The covariance matrix S = cov(Y) of the matrix Y can be represented by introducing a noise matrix R:

$$\boldsymbol{S = J \cdot R \cdot J^T} \quad (18)$$

where

$$J_{N-1,N}\begin{bmatrix} 1 & 0 & \vdots & 0 & -1 \\ 0 & 1 & \vdots & 0 & -1 \\ \vdots & \vdots & \ddots & \vdots & \vdots \\ 0 & 0 & 0 & \cdots & -1 \end{bmatrix} \tag{19}$$

By introducing the objective function and constraint based on Kuhn–Tucker theory, the underdetermined equations can be solved.

$$\boldsymbol{G}_{(\boldsymbol{r1N},\boldsymbol{r2N},\ldots,\boldsymbol{rNN})} = \frac{\mathbf{1}}{\boldsymbol{K}^2}\sum_{i<j}^{N}\boldsymbol{r}_{ij}^{2} \tag{20}$$

$$\boldsymbol{M}_{(\boldsymbol{r1N},\boldsymbol{r2N},\ldots,\boldsymbol{rNN})} = -\frac{|\boldsymbol{R}|}{|\boldsymbol{S}|\cdot\boldsymbol{K}} < \mathbf{0} \tag{21}$$

The initial value of the iterative calculation was set as follows:

$$\begin{cases} \boldsymbol{r}_{1N}^{0} = \mathbf{0}, \boldsymbol{i} < \boldsymbol{N} \\ \boldsymbol{r}_{NN}^{0} = \frac{\mathbf{1}}{\mathbf{2}\boldsymbol{S}^*}, \boldsymbol{S}^* = [\mathbf{1}\ \mathbf{1}\ \cdots\ \mathbf{1}]\boldsymbol{S}^{-1}[\mathbf{1}\ \mathbf{1}\ \cdots\ \mathbf{1}]^{\boldsymbol{T}} \end{cases} \tag{22}$$

To minimize the objective function under the constraints, N free parameters can be obtained. The R matrix can then be solved for, and the square root of its main diagonal elements is the uncertainty of each sequence:

$$\delta_i = \sqrt{r_{ij}} \tag{23}$$

4. Results

4.1. Validation of Modeled Daily ET with Ground Observations, PML_V2 ET, and SEBAL ET

The daily simulation outputs of TSEB-SM ET, PML_V2 ET, and SEBAL ET at Arou, Daman, Huazhaizi, and Sidaoqiao were compared with ground-based observations from 2014 to 2018, as shown in Figures 2 and 3. Figure 2 depicts the scatterplot of the three ET products compared to ground-based observations, and the validation metrics are shown in Table 1. Figure 3 illustrates that the products, which are derived from three distinct models, can all represent the intra-year single-peak trend of surface ET at the four ground observation sites. This trend displays ET at its lowest point at the beginning of the year, rising gradually with warmer temperatures and more precipitation until peaking in July and August. After September, when the crops are harvested and the leaves begin to wither, ET gradually declines until it reaches its lowest point at the end of the year, when it cycles again in the following year. However, the accuracy of the three products varied over the four sites. At the Arou site, the subsurface is dominated by alpine meadows with abundant rainfall, and the surface evapotranspiration fluctuates, with a high and pronounced peak that can reach up to 6 mm/d. The TSEB-SM ET product (R^2 of 0.79, RMSE of 0.76) was able to accurately capture the peak in comparison to the other two ET products. On the other hand, both the PML-V2 ET (R^2 of 0.76, RMSE of 0.78) and SEBAL ET (R^2 of 0.22, RMSE of 0.88) products displayed some underestimation, which was more noticeable for SEBAL ET, particularly during the middle of the growing season, when it occurred more frequently. But from January to March in the beginning of the year, SEBAL ET was overestimated. Furthermore, a number of 0 values in SEBAL ET did not match the real circumstances. In general, the SEBAL ET product was not very reliable at the Arou site, where there is a lot of rainfall, while the TSEB-SM ET product matched the ground-based data better.

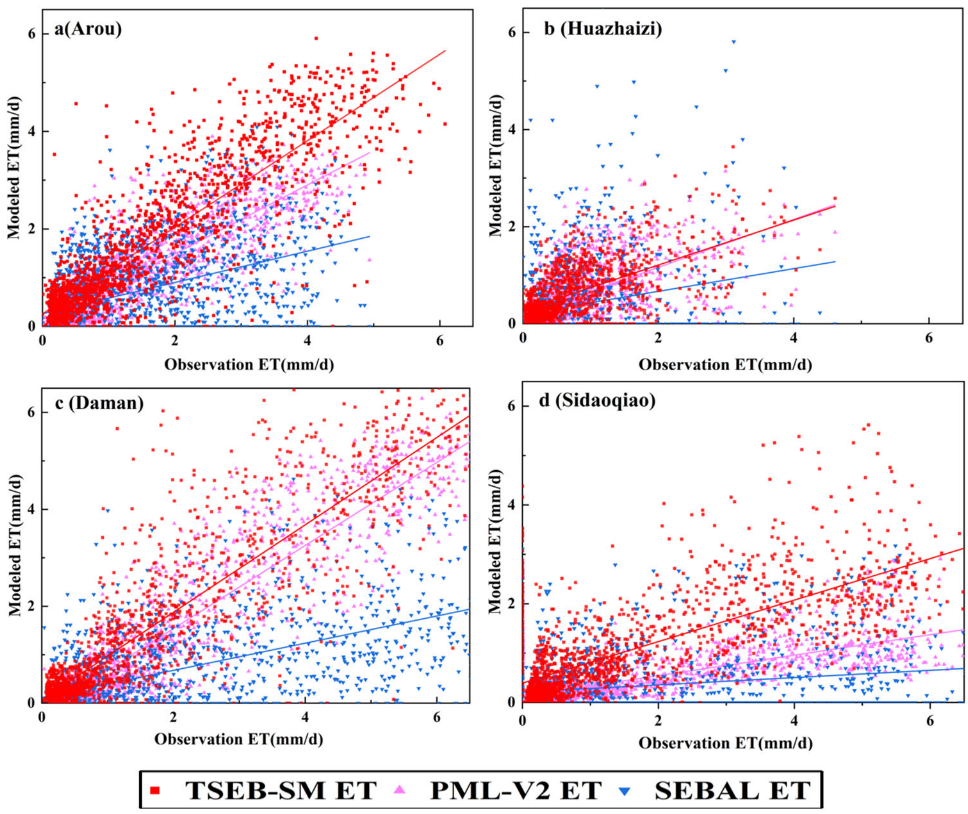

Figure 2. Scatterplot of TSEB-SM ET, PML-V2 ET, and SEBAL ET compared with ground observations.

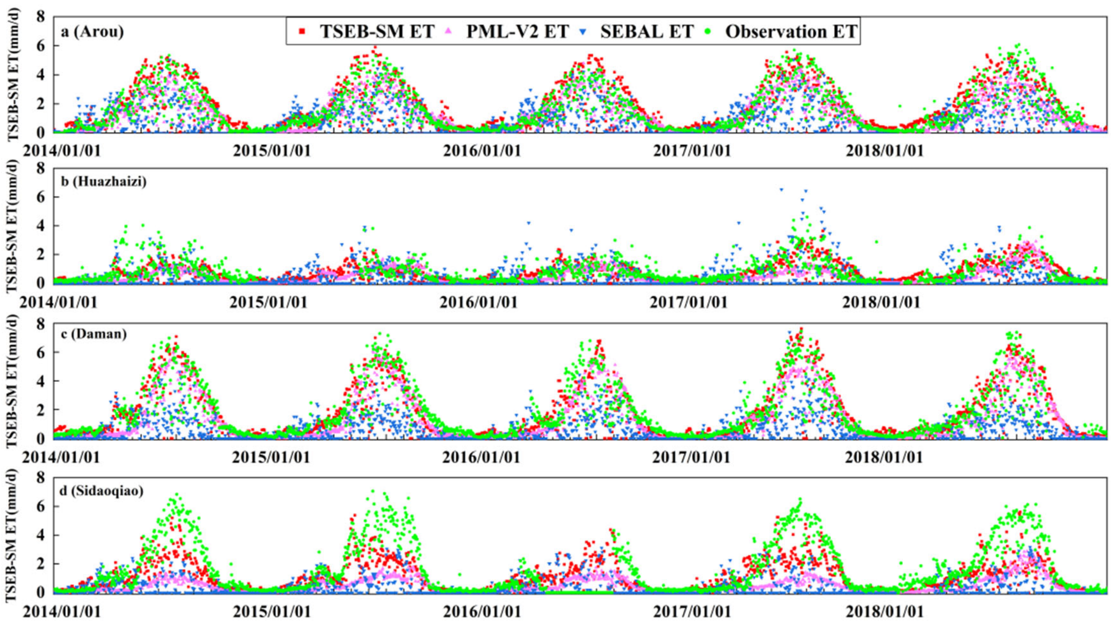

Figure 3. Temporal variations in the TSEB-SM ET, PML-V2 ET, and SEBAL ET (mm/d) against the observations for Arou (**a**), Huazhaizi (**b**), Daman (**c**), and Sidaoqiao (**d**).

Table 1. Metrics of the fit of the three ET products to the observations.

Site	Metrics	TSEB-SM	PML-V2	SEBAL
Arou	R^2	0.79	0.76	0.22
	RMSE(mm/d)	0.76	0.78	0.88
	Fitted equation	y = 0.91x + 0.32	y = 0.70x + 0.15	y = 0.32x + 0.32
Huazhaizi	R^2	0.38	0.39	0.05
	RMSE(mm/d)	0.46	0.47	0.74
	Fitted equation	y = 0.46x + 0.28	y = 0.49x + 0.17	y = 0.23x + 0.20
Daman	R^2	0.78	0.73	0.34
	RMSE(mm/d)	0.57	0.62	0.74
	Fitted equation	y = 0.90x + 0.07	y = 0.86x − 0.18	y = 0.28x + 0.12
Sidaoqiao	R^2	0.55	0.53	0.05
	RMSE(mm/d)	0.73	0.75	0.58
	Fitted equation	y = 0.42x + 0.39	y = 0.21x + 0.13	y = 0.07x + 0.21

The Huazhaizi site is situated in a desert area with irregular rainfall and low surface evapotranspiration, peaking at 4 mm/d. While the PML-V2 ET product underestimated the surface observations in 2017, it matched the surface observations to a greater extent in 2014, 2015, and 2016, and the TSEB-SM ET product better represented the real variability in surface ET at the Huazhaizi site. In the midst of the growing season, the SEBAL ET was more noticeable and still exhibited some values of 0, continuing to be overstated from January to March. The validation metrics are listed in Table 1.

The Daman site is in a highly irrigated agriculture area with great crop growth; therefore, its surface evapotranspiration fluctuates widely during the year, peaking at roughly 8 mm/d. The trajectory of the TSEB-SM ET product was the closest to that of the site observations (R^2 of 0.78, RMSE of 0.57), and it also had a peak at about 8 mm/d. PML-V2 ET followed the same trend as the site measurements to some extent (R^2 of 0.73, RMSE of 0.62), but it peaked significantly lower, at roughly 6 mm/d. During the growing season, SEBAL ET indicated a significant underestimate (R^2 of 0.34, RMSE of 0.74), with peak values of barely 4 mm/d. The TSEB-SM model adequately captured the large amount of water loss from the surface of the irrigated area during the early part of the growing season, allowing for a rapid response during that time and avoiding underestimation.

The Sidaoqiao site is located in the downstream riparian forest, and the surface ET intensity was moderate, with a peak around 6 mm/d. TSEB-SM ET, PML-V2 ET, and SEBAL ET were all underestimated to varying degrees during the growing season, with TSEB-SM ET being closest to the site observations, followed by PML-V2 ET (R^2 of 0.53, RMSE of 0.75), while SEBAL ET (R^2 of 0.05, RMSE of 0.58) showed the largest deviation from the ground-based site observations. Overall, comparing the three ET products with the ground observations, TSEB-SM ET performed the best and had the closest fit to the ground observations (R^2 of 0.55, RMSE of 0.73).

4.2. Temporal Dynamics of Annual Cumulative ET in the Study Area

Significant spatial discrepancies are highlighted in Figure 4, which depicts the regional characteristics in yearly cumulative ET in the Heihe River Basin from 2000 to 2020. There were significant variations in ET between the midstream irrigation area and the downstream Gobi Desert (up to 600 mm/year), with the annual total ET in the study region ranging from 100 to 750 mm/year. The midstream irrigated oasis zone showed the highest yearly cumulative ET, while the downstream Gobi Desert region showed the least ET. There are a great deal of summer precipitation, significant fluctuations in temperature, and rapid evaporation in the upstream watershed of the Qilian Mountains region. The midstream Hexi Corridor region experiences a drier climate than the upstream regions. Despite being in a dry and semi-arid area with little precipitation, the midstream artificial oasis region (around 40°N) has the strongest ET. The reason for this is that there are many irrigated agricultural regions that are supplied with water from reservoirs in the Qilian Mountains, and these dry climatic circumstances lead to an intense need for atmospheric evaporation. All of the downstream areas are covered by the Gobi Desert except for a small amount of oasis existing along the Heihe River, and the downstream area has low precipitation and strong evaporation, so ET is mainly provided by soil evaporation, but the ET here is the lowest in the study area. The interannual fluctuations in ET in the Heihe River Basin from 2000 to 2020 were not very significant, with little year-to-year variation. In addition to the relatively stable climate and precipitation in the study area, it is also inseparable from the active water management initiatives undertaken by the local government. In May 2000, in response to ecological problems such as the drying up of rivers and lakes, death of forests, and rampant sandstorms in the Heihe River Basin, the government departments concerned carried out water dispatching work for the main stream of the Heihe River to reasonably manage water usage along the Heihe River Basin, thus reducing the occurrence of cutoffs. In September 2001, a severe drought was experienced in the midstream region, but the impact of this drought on the midstream region was reduced by a reasonable allocation of water.

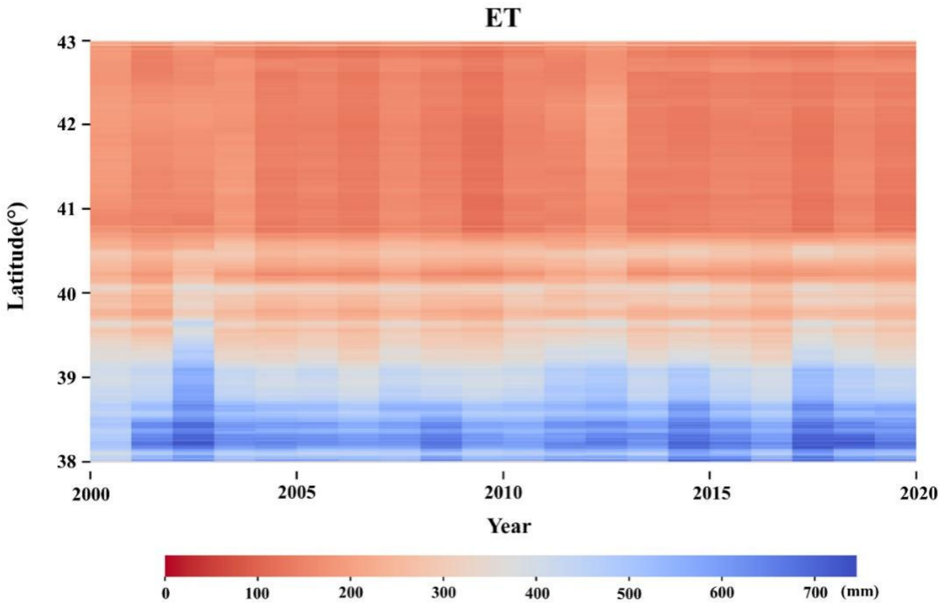

Figure 4. Spatial distribution of annual cumulative ET modeled by TSEB-SM.

5. Discussion

5.1. Relative Uncertainty from TCH

Figure 5 illustrates the pixel-by-pixel relative uncertainty and statistical histograms of the TSEB-SM, PML-V2, and SEBAL ET products in the Heihe River Basin. Overall, the TSEB-SM and PML-V2 products have substantially smaller relative uncertainty than SEBAL ET. From the statistical histograms, it appears that most of the relative uncertainty values for TSEB-SM ET are distributed between 50 and 70%, those for PML-V2 ET are mainly in the range of 70–90%, and those for SEBAL ET are in the range of 60–70% in the upstream portion of the region, with most of the rest exceeding 200%. The high relative uncertainty values of TSEB-SM ET are mostly distributed in the downstream arid Gobi area and a few grassland areas in the upstream and midstream. Most of the high relative uncertainty values of PML-V2 ET are distributed in the downstream Gobi Desert region, with some being distributed in the midstream irrigation regions and upstream alpine meadow region. The high relative uncertainty values for SEBAL ET are also predominantly distributed in the downstream and midstream regions. This is similar to the results of the previous (Section 4.1) comparison with the ground station observations, where all three products were underestimated in the downstream, resulting in high relative uncertainties.

It is worth noting that TSEB-SM ET has lower relative uncertainty in the midstream irrigation region compared to the upstream alpine meadow region. This is primarily due to the input of soil moisture into the TSEB-SM model, which monitors the large amount of water depletion in the yield of the early crop-growing season and, thus, simulates surface evapotranspiration with greater accuracy. Also, the relative uncertainties of all three products are lower in the upstream of the Heihe River Basin, which is mainly due to the fact that the upstream is primarily alpine meadows with abundant rainfall, and for both TSEB-SM ET and PML-V2 ET based on the energy balance and PML-V2 ET based on the P-M equations of the physical model, a better simulation of surface evapotranspiration can be carried out. Generally, TSEB-SM ET outperformed PML-V2 ET and SEBAL ET in arid and semi-arid regions at the watershed scale.

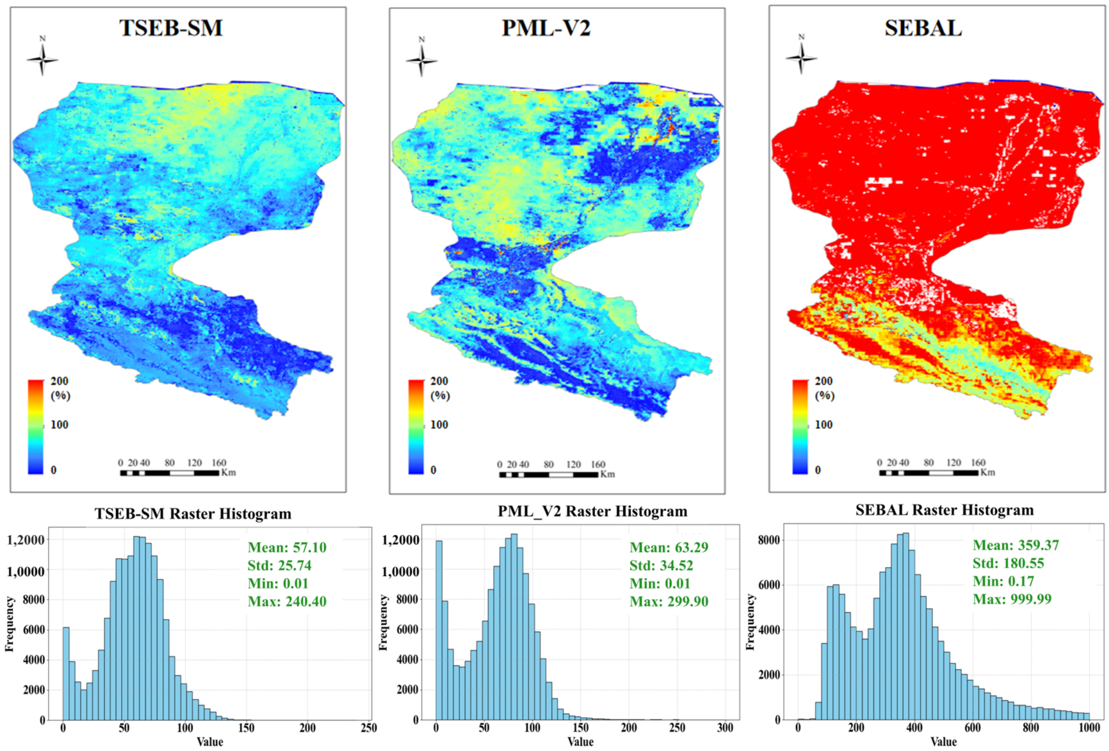

Figure 5. The spatial distributions of the relative uncertainties of the 3 ET products over the Heihe River Basin.

5.2. Temporal Dynamics of Annual Cumulative ET in the Study Area Based TSEB-SM, PML_V2, and SEBAL

The spatial distribution of the annual cumulative ET of TSEB-SM (2001–2018) was compared with that of PML-V2 (2001–2018) and SEBAL (2001–2018) over the whole of the Heihe River Basin (Figure 6). Although these three satellite-based ET products show generally similar spatial patterns across the Heihe River Basin, regions of divergence can also be seen, particularly in the upstream and midstream parts of the catchment. The TSEB-SM products provided annual ET in the range of 400–700 mm/year in the alpine meadows in the upstream area, while PML-V2 and SEBAL provided a much lower range of 300–500 mm/year. The TSEB-SM and PML-V2 products provided annual ET ranges in the artificial "oasis" irrigation region of 500–700 mm/year and 400–600 mm/year, respectively, which are quite close to the ground-based estimate (range 500–650 mm/year) (Figures 3 and 4). In contrast, SEBAL provided lower annual ET values of 300–500 mm/year in this area.

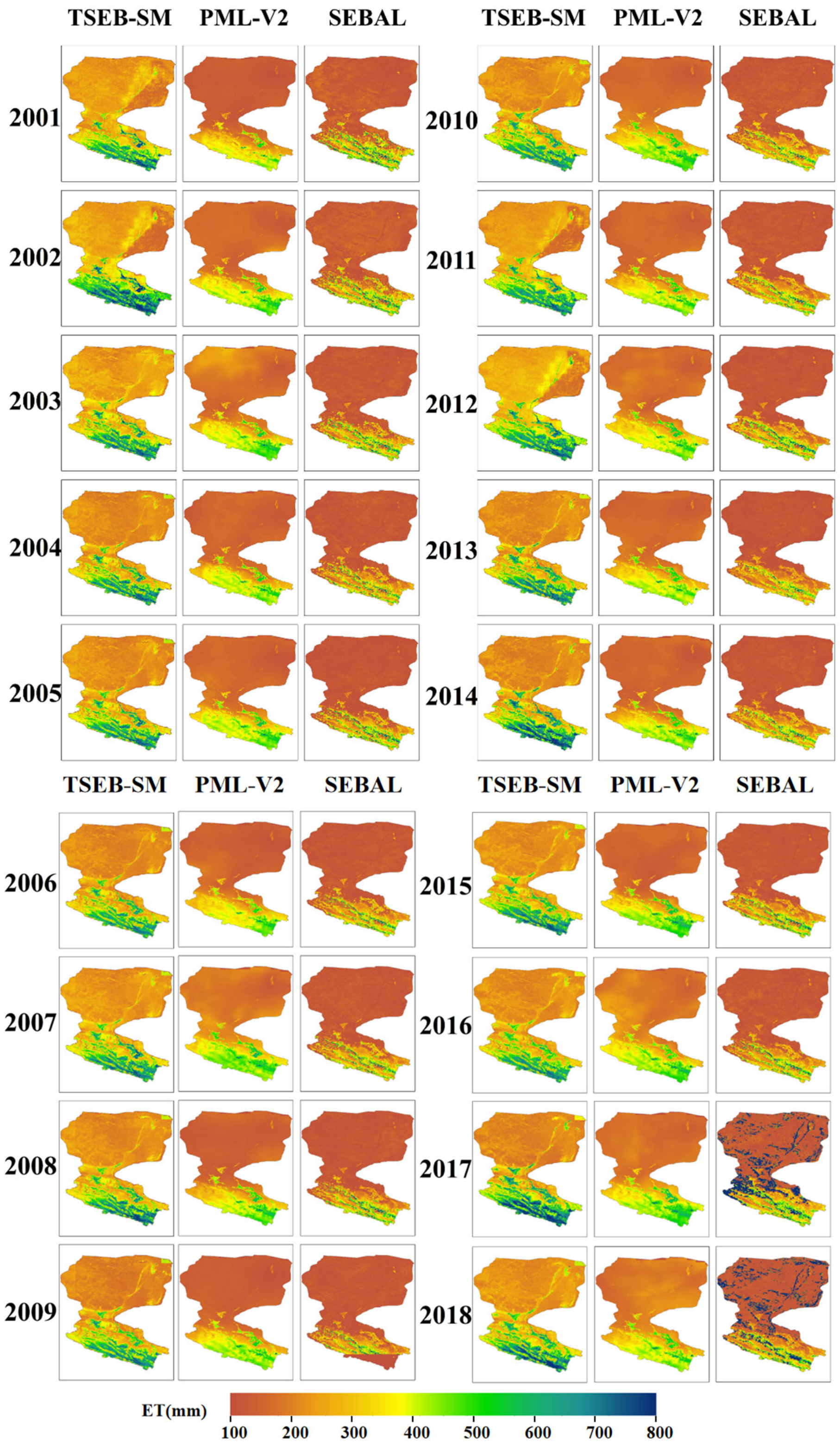

Figure 6. Variations in annual ET estimates by TSEB-SM, PML-V2, and SEBAL from 2001 to 2018 across the Heihe River Basin.

The variation in the annual ET in the Heihe River Basin is mainly driven by changing precipitation in the up- and midstream areas, as well as by the impacts of changing irrigation regimes in the midstream. The measured precipitation in the upstream areas showed an increasing trend over the years 2001–2018, and this resulted in an increase in annual ET, which was captured by the TSEB-SM and PML-V2 ET products. In contrast, the SEBAL ET product showed an insignificant change from 2001 to 2018 (except for the wrong value in the downstream).

The comparison of the three ET products for seasonal trends in ET and the intercomparison of spatial patterns of ET across the Heihe Basin suggest that the water balance in the well-watered agricultural and grassland areas is more accurately captured by the TSEB-SM model than by the other two satellite-based ET products (Figure 7). The improvements shown by the TSEB-SM model in this catchment are due to the way in which it not only correctly captures the large water loss from the land surface in the early growing season, which is often missed by traditional stomatal conductance or process-based models, but also addresses the underestimation of ET in the peak growing season shown by other satellite-based ET products [33,34]. The underestimation of ET in the peak plant growing season appears to be mainly due to the simplified parametrization of canopy stomatal conductance [11,35].

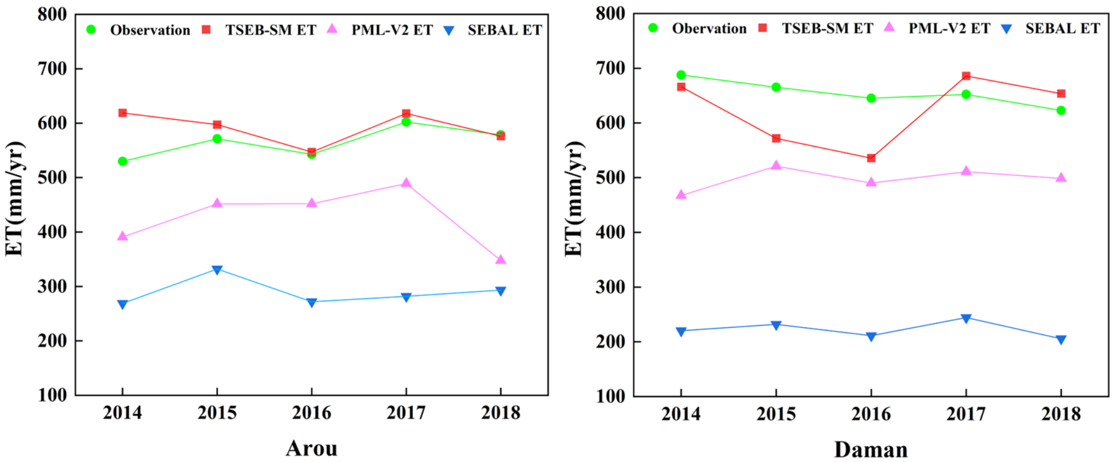

Figure 7. The annual ET of three products and observations from 2014 to 2018 at the Arou and Daman sites.

5.3. Limitations in Modeling ET under Sparse Vegetation Cover Conditions

The generated daily ET data produced by TSEB-SM showed good agreement with the ground measurements at the grassland and cropland sites with relatively homogeneous surface conditions, but TSEB-SM did not generate fully reliable estimates of ET over sparse vegetation cover conditions, where the modeled daily ET did not capture intermittent high values in rainy days at the Huazhaizi site and peak values that occurred during the middle of the growing season at the Sidaoqiao site. The TSEB-SM model yielded better performance at these dry surface sites when using more accurate surface soil moisture data such as ground measurements or SMAP retrievals as model inputs [36,37]. This indicates that the deficiencies in the TSEB-SM product reported here are primarily due to the satellite soil moisture data input to the model.

The model inputs of soil moisture (2003–2019) were derived by downscaling the microwave soil moisture products of AMSR-E and AMSR-2 (which have an extremely coarse spatial resolution of 36 km) down to 1 km using the MODIS reflectance and LST data. The rapid increases in soil moisture introduced by rainfall events were not captured by the microwave observations in the region of interest. This is because rainfall is not necessarily region-wide in these areas, so rain-covered areas are likely to be of a different scale when compared to the coarse-resolution microwave soil moisture products driving the downscaling. Underestimates in the downscaled soil moisture contributed to the underestimation of daily ET at the high points when the rainfall events occurred at the Huazhaizi site. In addition, in the coarse microwave satellite pixel where the Sidaoqiao site is located, the flux tower was installed in a shrubland area surrounded by sparse woodland and very dry bare soil as land cover. These dry surfaces result in lower soil moisture values derived by AMSR-E and AMSR-2 when compared with the value derived from a SMAP pixel that mostly consists of vegetation-covered land cover around the flux tower. As a result of spatial mismatching, the downscaled soil moisture data used in this study were lower than those downscaled from SMAP soil moisture products. For the purposes of this long-duration study, the only soil moisture products available for 2000–2020 were the AMSR-E and AMSR-2 microwave products.

6. Conclusions

In this study, TSEB-SM and a temporal upscaling method were used to produce spatiotemporally continuous daily ET data with a spatial resolution of 1 km across the Heihe River Basin for a lengthy time period from 2000 to 2020, combined with ground-based observations and other ET products for comparison and validation. The results were as follows:

(1) The performance of the three ET products varied at different stations in the Heihe River Basin (in the order of TSEB-SM, PML-V2, and SEBAL ET). At Arou station, the R^2 of the three products was 0.79, 0.76 and 0.22, respectively, with RMSE of 0.76 mm/d, 0.78 mm/d, and 0.88 mm/d, respectively. At Daman station, the R^2 values were 0.78, 0.73, and 0.34, respectively, and the RMSE values were 0.57 mm/d, 0.62 mm/d, and 0.74 mm/d, respectively.

(2) According to our findings, there are significant spatial differences in ET in the Heihe River Basin, with the annual total ET in the study region ranging from 100 to 750 mm/year. The midstream irrigated oasis zone showed the largest yearly cumulative ET (about 700 mm/year), while the downstream Gobi Desert region showed the least ET (about 100 mm/year).

(3) From the results of the TCH analysis, the TSEB-SM and PML-V2 ET models showed substantially smaller relative uncertainty than the SEBAL ET model. Most of the relative uncertainty values for TSEB-SM ET were distributed between 50 and 70%, those for PML-V2 ET were mainly in the range of 70–90%, and those for SEBAL ET ranged from 60 to 70% and were predominantly distributed in the upstream. Generally, TSEB-SM ET outperformed PML-V2 ET and SEBAL ET in arid and semi-arid regions at the watershed scale.

Supplementary Materials: The following supporting information can be downloaded at: https://www.mdpi.com/article/10.3390/rs16030462/s1.

Author Contributions: This paper is a collaborative work by all of the authors. Conceptualization, L.S.; Data Curation, S.T.; Formal Analysis, S.T.; Methodology, S.T. and L.S.; Supervision, S.T., L.S., L.Z. and G.Z.; Writing—Original Draft, S.T.; Writing—Review and Editing, S.T., L.S. and L.Z. All authors have read and agreed to the published version of the manuscript.

Funding: This work was supported by the National Natural Science Foundation of China (42071298) and the Anhui Province's University Science Project for Distinguished Young Scholars (2022AH030025).

Data Availability Statement: We gratefully acknowledge all people who participated in the EC measurements, and we have shared the measured data on the platform of the National Tibetan Plateau Data Center (https://data.tpdc.ac.cn/).

Conflicts of Interest: The authors declare that they have no conflicts of interest to disclose.

References

1. Jung, M.; Reichstein, M.; Ciais, P.; Seneviratne, S.I.; Sheffield, J.; Goulden, M.L.; Bonan, G.; Cescatti, A.; Chen, J.Q.; de Jeu, R.; et al. Recent decline in the global land evapotranspiration trend due to limited moisture supply. *Nature* **2010**, *467*, 951–954. [CrossRef] [PubMed]
2. Jasechko, S.; Sharp, Z.D.; Gibson, J.J.; Birks, S.J.; Yi, Y.; Fawcett, P.J. Terrestrial water fluxes dominated by transpiration. *Nature* **2013**, *496*, 347–350. [CrossRef] [PubMed]
3. Trenberth, K.E.; Fasullo, J.T.; Kiehl, J. Earth's global energy budget. *Bull. Am. Meteorol. Soc.* **2009**, *90*, 311–324. [CrossRef]

4. Schumacher, D.L.; Keune, J.; van Heerwaarden, C.C.; de Arellano, J.V.G.; Teuling, A.J.; Miralles, D.G. Amplification of mega-heatwaves through heat torrents fuelled by upwind drought. *Nat. Geosci.* **2019**, *12*, 712–717. [CrossRef]
5. Forzieri, G.; Alkama, R.; Miralles, D.G.; Cescatti, A. Satellites reveal contrasting responses of regional climate to the widespread greening of Earth. *Science* **2017**, *356*, 1140–1144. [CrossRef]
6. Dinpashoh, Y. Study of reference crop evapotranspiration in IR of Iran. *Agric. Water Manag.* **2006**, *84*, 123–129. [CrossRef]
7. Allen, R.; Irmak, A.; Trezza, R.; Hendrickx, J.M.H.; Bastiaanssen, W.; Kjaersgaard, J. Satellite-based ET estimation in agriculture using SEBAL and METRIC. *Hydrol. Process.* **2011**, *25*, 4011–4027. [CrossRef]
8. Bastiaanssen, W.G.M.; Pelgrum, H.; Wang, J.; Ma, Y.; Moreno, J.F.; Roerink, G.J.; van der Wal, T. A remote sensing surface energy balance algorithm for land (SEBAL)—2. Validation. *J. Hydrol.* **1998**, *212*, 213–229. [CrossRef]
9. Yang, Y.; Shang, S.; Jiang, L. Remote Sensing Temporal and Spatial Patterns of Evapotranspiration and the Responses to Water Management in a Large Irrigation District of North China. In *Evapotranspiration Over Heterogeneous Vegetated Surfaces: Models and Applications*; Springer: Berlin/Heidelberg, Germany, 2015; pp. 109–127.
10. Yebra, M.; Van Dijk, A.; Leuning, R.; Huete, A.; Guerschman, J.P. Evaluation of optical remote sensing to estimate actual evapotranspiration and canopy conductance. *Remote Sens. Environ.* **2013**, *129*, 250–261. [CrossRef]
11. He, S.Y.; Zhang, Y.Q.; Ma, N.; Tian, J.; Kong, D.D.; Liu, C.M. A daily and 500 m coupled evapotranspiration and gross primary production product across China during 2000–2020. *Earth Syst. Sci. Data* **2022**, *14*, 5463–5488. [CrossRef]
12. Yao, Y.J.; Liang, S.L.; Li, X.L.; Hong, Y.; Fisher, J.B.; Zhang, N.N.; Chen, J.Q.; Cheng, J.; Zhao, S.H.; Zhang, X.T.; et al. Bayesian multimodel estimation of global terrestrial latent heat flux from eddy covariance, meteorological, and satellite observations. *J. Geophys. Res. Atmos.* **2014**, *119*, 4521–4545. [CrossRef]
13. Cheng, G.D.; Li, X.; Zhao, W.Z.; Xu, Z.M.; Feng, Q.; Xiao, S.C.; Xiao, H.L. Integrated study of the water-ecosystem-economy in the Heihe River Basin. *Natl. Sci. Rev.* **2014**, *1*, 413–428. [CrossRef]
14. Li, X.; Cheng, G.D.; Ge, Y.C.; Li, H.Y.; Han, F.; Hu, X.L.; Tian, W.; Tian, Y.; Pan, X.D.; Nian, Y.Y.; et al. Hydrological Cycle in the Heihe River Basin and Its Implication for Water Resource Management in Endorheic Basins. *J. Geophys. Res. Atmos.* **2018**, *123*, 890–914. [CrossRef]
15. Yang, Y.; Chen, R.S.; Song, Y.X.; Liu, J.F.; Han, C.T.; Liu, Z.W. Measurement and estimation of grassland evapotranspiration in a mountainous region at the upper reach of Heihe River basin, China. *Chin. J. Appl. Ecol.* **2013**, *24*, 1055–1062.
16. Song, K.C.; Kang, E.S.; Jin, B.W.; Zhang, Z.H. An Experimental Study of Grassland Evapotranspiration in the Mountain Watershed of the Hei River Basin. *J. Glaciol. Geocryol.* **2004**, *3*, 349–356.
17. Zhang, X.D.; Zhou, J.; Liang, S.L.; Wang, D.D. A practical reanalysis data and thermal infrared remote sensing data merging (RTM) method for reconstruction of a 1-km all-weather land surface temperature. *Remote Sens. Environ.* **2021**, *260*, 112437. [CrossRef]
18. Xiao, Z.Q.; Liang, S.L.; Wang, J.D.; Chen, P.; Yin, X.J.; Zhang, L.Q.; Song, J.L. Use of General Regression Neural Networks for Generating the GLASS Leaf Area Index Product from Time-Series MODIS Surface Reflectance. *IEEE Trans. Geosci. Remote Sens.* **2014**, *52*, 209–223. [CrossRef]
19. Pan, X.D.; Li, X.; Shi, X.K.; Han, X.J.; Luo, L.H.; Wang, L.X. Dynamic downscaling of near-surface air temperature at the basin scale using WRF-a case study in the Heihe River Basin, China. *Front. Earth Sci.* **2012**, *6*, 314–323. [CrossRef]
20. Foken, T. The energy balance closure problem: An overview. *Ecol. Appl.* **2008**, *18*, 1351–1367. [CrossRef] [PubMed]
21. Cheng, M.H.; Jiao, X.Y.; Li, B.B.; Yu, X.; Shao, M.C.; Jin, X.L. Long time series of daily evapotranspiration in China based on the SEBAL model and multisource images and validation. *Earth Syst. Sci. Data* **2021**, *13*, 3995–4017. [CrossRef]
22. Norman, J.; Kustas, W.; Humes, K. Source approach for estimating soil and vegetation energy fluxes in observations of directional radiometric surface temperature. *Agric. For. Meteorol.* **1996**, *2*, 297. [CrossRef]
23. Andreu, A.; Kustas, W.P.; Polo, M.J.; Carrara, A.; González-Dugo, M.P. Modeling surface energy fluxes over a dehesa (oak savanna) ecosystem using a thermal based two-source energy balance model (TSEB) I. *Remote Sens.* **2018**, *10*, 558. [CrossRef]
24. Chávez, J.L.; Gowda, P.H.; Howell, T.A.; Neale, C.M.U.; Copeland, K.S. Estimating hourly crop ET using a two-source energy balance model and multispectral airborne imagery. *Irrig. Sci.* **2009**, *28*, 79–91. [CrossRef]
25. Xue, K.J.; He, M.; Bian, Z.J.; Song, L.S.; XU, Y.H.; Jiang, H. Estimating instantaneous evapotranspiration based on dual-angle thermal infrared observations from Sentinel-3 satellite. *Natl. Remote Sens. Bull.* **2021**, *25*, 1683–1699. [CrossRef]
26. Priestley, C.H.B.; Taylor, R.J. On the assessment of surface heat flux and evaporation using large-scale parameters. *Mon. Weather Rev.* **1972**, *100*, 81–92. [CrossRef]
27. De Kauwe, M.G.; Kala, J.; Lin, Y.S.; Pitman, A.J.; Medlyn, B.E.; Duursma, R.A.; Abramowitz, G.; Wang, Y.P.; Miralles, D.G. A test of an optimal stomatal conductance scheme within the CABLE land surface model. *Geosci. Model Dev.* **2015**, *8*, 431–452. [CrossRef]
28. Song, L.S.; Kustas, W.P.; Liu, S.M.; Colaizzi, P.D.; Nieto, H.; Xu, Z.W.; Ma, Y.F.; Li, M.S.; Xu, T.R.; Agam, N.; et al. Applications of a thermal-based two-source energy balance model using Priestley-Taylor approach for surface temperature partitioning under advective conditions. *J. Hydrol.* **2016**, *540*, 574–587. [CrossRef]
29. Merlin, O.; Al Bitar, A.; Rivalland, V.; Béziat, P.; Ceschia, E.; Dedieu, G. An Analytical Model of Evaporation Efficiency for Unsaturated Soil Surfaces with an Arbitrary Thickness. *J. Appl. Meteorol. Clim.* **2010**, *50*, 457–471. [CrossRef]
30. Bowen, I.S. The ratio of heat losses by conduction and by evaporation from any water surface. *Phys. Rev.* **1926**, *27*, 779–787. [CrossRef]

31. Premoli, A.; Tavella, P. A revisited 3-cornered hat method for estimating frequency standard instability. *IEEE Trans. Instrum. Meas.* **1993**, *42*, 7–13. [CrossRef]
32. Tavella, P.; Premoli, A. Estimating the instabilities of n-clocks by measuring differences of their readings. *Metrologia* **1994**, *30*, 479–486. [CrossRef]
33. Shang, K.; Yao, Y.J.; Liang, S.L.; Zhang, Y.H.; Fisher, J.B.; Chen, J.Q.; Liu, S.M.; Xu, Z.W.; Zhang, Y.; Jia, K.; et al. DNN-MET: A deep neural networks method to integrate satellite-derived evapotranspiration products, eddy covariance observations and ancillary information. *Agric. For. Meteorol.* **2021**, *308–309*, 108582. [CrossRef]
34. Zhang, Y.; Liu, S.M.; Song, L.S.; Li, X.; Jia, Z.Z.; Xu, T.R.; Xu, Z.W.; Ma, Y.F.; Zhou, J.; Yang, X.F.; et al. Integrated Validation of Coarse Remotely Sensed Evapotranspiration Products over Heterogeneous Land Surfaces. *Remote Sens.* **2022**, *14*, 3467. [CrossRef]
35. Zhang, Y.Q.; Pena-Arancibia, J.L.; McVicar, T.R.; Chiew, F.H.S.; Vaze, J.; Liu, C.M.; Lu, X.J.; Zheng, H.X.; Wang, Y.P.; Liu, Y.Y.; et al. Multi-decadal trends in global terrestrial evapotranspiration and its components. *Sci. Rep.* **2016**, *6*, 19124. [CrossRef]
36. Song, L.; Ding, Z.; Kustas, W.P.; Xu, Y.; Zhao, G.; Liu, S.; Ma, M.; Xue, K.; Bai, Y.; Xu, Z. Applications of a thermal-based two-source energy balance model coupled to surface soil moisture. *Remote Sens. Environ.* **2022**, *271*, 112923. [CrossRef]
37. Xu, Y.; Song, L.; Kustas, W.P.; Xue, K.; Liu, S.; Ma, M.; Xu, T.; Zhao, L. Application of the two-source energy balance model with microwave-derived soil moisture in a semi-arid agricultural region. *Int. J. Appl. Earth Obs. Geoinf.* **2022**, *112*, 102879. [CrossRef]